Non-destructive monitoring of internal temperature distribution in prismatic Li-ion battery cells with ultrasound tomography[1]

*Shengyuan Zhang Peng Zuo Zheng Fan**

Shengyuan Zhang
School of Mechanical and Aerospace Engineering, Nanyang Technological University, Singapore 639798
Peng Zuo
Advanced Remanufacturing and Technology Centre (ARTC), Agency for Science, Technology and Research (A*STAR), Singapore 637143
Zheng Fan
School of Mechanical and Aerospace Engineering, Nanyang Technological University, Singapore 639798
Email Address: zfan@ntu.edu.sg

Keywords: *Electric vehicle, energy storage system, lithium-ion battery, thermal management, ultrasound tomography*

Large prismatic cells are increasingly being used as the primary power source in transportation applications. Effective online thermal management of these cells is crucial for ensuring safety and maximizing performance. However, significant discrepancies between surface and internal temperatures make it difficult to detect internal thermal anomalies promptly, which hinders effective thermal management and increases the risk of irreversible thermal hazards. This paper introduces an innovative technology for thermal management in prismatic Li-ion batteries. By exploiting the temperature sensitivity of ultrasound velocity and applying tomographic reconstruction based on surrounding measurements, the technology enables detailed cross-sectional thermal imaging. This allows for non-destructive, real-time visualization of internal temperatures. Furthermore, with its compact design and cost-effectiveness, this technology is suitable for in-situ deployment, offering a precise feedback mechanism for online thermal management. Demonstrations conducted during continuous discharging scenarios have shown that the system can identify high-temperature regions near the tabs that remain undetected by surface thermocouples. This advancement has the potential to significantly reduce the risk of fires or explosions while enhancing battery performance in electric vehicles and other applications involving battery cells.

1 Introduction

Large prismatic Li-ion battery cells are extensively employed in transportation applications, where maintaining an optimal operating temperature is critical for ensuring safety. Excessive temperatures can trigger irreversible thermal runaway [1, 2], potentially leading to hazardous outcomes such as fires or explosions. Conversely, operating batteries in cold environments can induce lithium plating, which also elevates the risk of thermal runaway [3, 4, 5].
Temperature regulation is equally vital for optimizing battery performance. At low temperatures, reduced electrolyte conductivity and sluggish lithium-ion diffusion result in voltage drops and capacity loss [6]. While fast charging is a key requirement for high-performance batteries, it becomes increasingly challenging at low temperatures due to the heightened risk of lithium plating. Pre-heating is therefore essential to mitigate lithium plating [7] and reduce charging time [8]. On the other hand, continuous fast charging and discharging generate excessive heat [9], necessitating active cooling in later stages to maintain a safe operating temperature.
Beyond immediate safety and performance concerns, temperature plays a pivotal role in battery aging [10]. At low temperatures, lithium plating accelerates capacity degradation. Conversely, high temperatures can also hasten capacity degradation by promoting the growth and repair of the solid electrolyte interphase (SEI) layer [11]. Implementing a precise, long-term battery management strategy can significantly extend battery life [12].
Effective thermal management hinges on accurate temperature measurements. While surface temperature measurements using thermocouples and thermal imaging systems are relatively straightforward, they often fail to capture critical internal thermal anomalies. Under abusive conditions, internal short circuits can generate localized high-temperature regions [13, 14, 15], which can rapidly escalate to thermal runaway [16]. Early detection of these internal thermal anomalies is essential for preventing thermal

[1]Part of the data and code are provided to reproduce the results presented in Figure 6 and Movie S6. See DOI: 10.17632/pd464vmmpg.1.

runaway, rather than relying on surface measurements that only identify the issue after it has occurred [17].

Even under normal operating conditions, large prismatic battery designs exhibit significant temperature differences between the interior and surface. Self-heating during operation can substantially increase internal temperatures, while heat dissipation is impeded by the battery's multilayered structure and the low thermal conductivity of its components [18, 19]. This can lead to substantial temperature gradients, with differences of up to 26.2 °C across the thickness of a 280 Ah prismatic cell [20]. Furthermore, during fast charging or discharging, current concentration near the tabs creates non-uniform in-plane temperature distributions [21, 22, 23, 24, 25, 26, 27]. These thermal inhomogeneities not only compromise safety and performance but also accelerate uneven degradation [28, 29], underscoring the importance of internal temperature measurements [30] to ensure an optimal thermal state throughout the cell.

In practice, thermocouples are often attached to the negative or positive poles to estimate the highest internal temperature under normal operating conditions. However, this method does not provide an accurate representation of internal temperature [22, 24, 25] and is ineffective under abnormal conditions. A recent study [31] employed X-ray diffraction for internal temperature measurement, but this approach is unsuitable for in-situ monitoring. Existing in-situ internal temperature monitoring technologies can be broadly categorized into three main approaches: embedded thermal sensors, model-based estimation, and impedance-based estimation [18]. Temperature sensors, such as resistance temperature detectors (RTDs) [32, 33], thermocouples [20, 21, 34], and fiber Bragg grating (FBG) sensors [35, 36], are embedded within Li-ion batteries to measure temperature directly. However, these sensors inevitably degrade battery performance. Alternatively, model-based methods predict internal temperature using measurable parameters like current and voltage, but these models often struggle to balance accuracy and efficiency in complex scenarios [37]. Another non-destructive approach involves estimating internal temperature based on electrochemical impedance, a temperature-dependent parameter. However, this method only provides an average temperature [37], whereas real-world applications typically involve uneven temperature distributions with significant differences between maximum/minimum and average temperatures. In-situ and non-destructive internal temperature monitoring remains a critical challenge for effective online thermal management of prismatic cells [38].

Non-destructive testing using penetrative ultrasonic waves has emerged as a promising tool for estimating the internal state of batteries [39]. In addition to being non-destructive, ultrasonic testing is low-power, efficient, compact, affordable, and standalone, making it well-suited for in-situ and real-time monitoring tasks. Recent studies have demonstrated the sensitivity of ultrasonic features to internal temperatures [40, 41, 42], suggesting that ultrasound can be used to diagnose internal temperature.

To map temperature distribution and detect abnormal thermal events at any location, ultrasound tomography, which has proven valuable in applications such as breast cancer screening [43, 44], emerges as a strong candidate. This technique provides fast, non-destructive cross-sectional imaging by projecting ultrasonic waves from various angles in a two-dimensional space. As these waves traverse an object, their features, such as amplitude and travel time, change in response to the object's internal properties along the wave's path. Tomographic reconstruction is then employed to compute the distribution of acoustic properties within the imaging region, such as sound speed and acoustic attenuation. Since acoustic properties correlate directly with temperature, the temperature distribution can be inferred from the acoustic property distribution [45, 46].

Therefore, the objective of this paper is to develop a customized ultrasound tomography system for monitoring internal temperatures in prismatic cells. This system is designed to be low-power, compact, cost-effective, non-destructive, and highly efficient, enabling in-situ and real-time internal temperature monitoring for each cell in electric vehicles, as illustrated in Figure 1. This technology would serve as a groundbreaking feedback mechanism for thermal management systems, ensuring optimal working conditions and reducing the risk of thermal runaway in batteries.

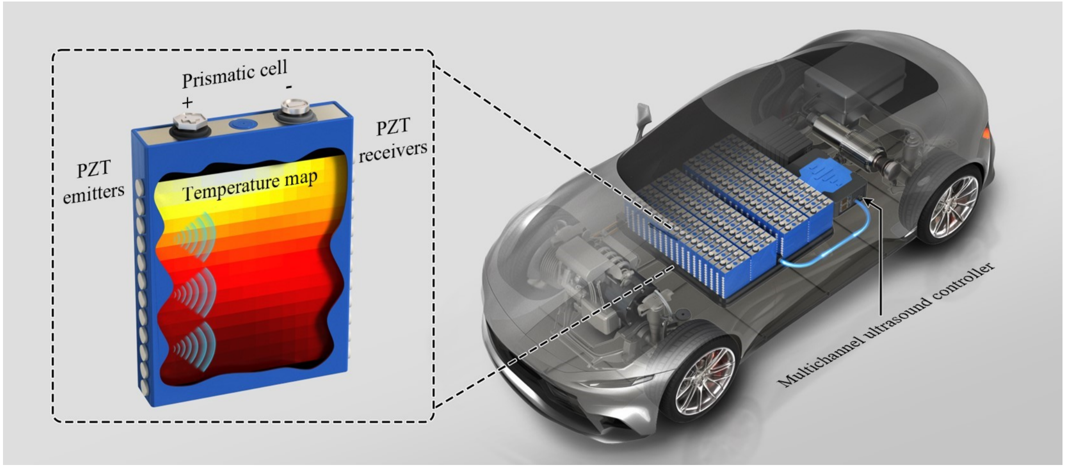

Figure 1: Schematic of in-situ monitoring of the internal temperature distribution within each cell of an electric vehicle using an ultrasound tomography system.

2 Results

2.1 Configuration of the imaging system

Ultrasound tomography enables cross-sectional imaging using ultrasonic transducers arranged around the cross-section. These transducers emit unfocused cylindrical ultrasonic waves and receive the transmitted waves, ensuring full coverage of the cross-section.
The prismatic cell used for demonstration is a commercial $LiFePO_4$ prismatic cell with a rated capacity of 50Ah (EVE LF50K). As visualized by the X-ray CT in Figure 2A, the prismatic cell contains two rolls of prismatically winded electrode/separator layers.
The imaging cross-section is in the plane of the mid-layers of an electrode roll. This plane was selected for several reasons: 1) Thermal abnormalities typically occur internally. 2) The mid-layer plane is mostly homogeneous, simplifying wave propagation. Conversely, if the imaging plane is parallel to the side or bottom views, with ultrasonic transducers on the front and back surfaces, the wave propagation path becomes highly inhomogeneous, causing strong refraction due to the inclined transmission of the layers. 3) Electrolyte gaps at the side corners necessitate placing ultrasonic transducers on the mid-layer plane, where the gap thickness is minimal, to promote transmission through the gap.
Given the rectangular cross-section, ultrasonic transducers should be arranged in four linear arrays, each placed on one side of the cross-section to achieve a complete range of projection angles for tomography. However, the presence of the electrolyte/air region at the top of the cell and the electrolyte gaps at the corners and bottom hampers effective ultrasonic wave transmission. High-quality signals can only be obtained from the left and right sides of the mid-layer plane. Consequently, only two arrays of ultrasonic transducers are used, with one set of transducers acting as emitters on one side of the battery and another set acting as receivers on the opposing side, creating a parallel setup. This configuration results in a typical limited-angle tomography problem.
As illustrated in Figure 2B, the plane of imaging is not fully homogeneous. At both the left and right sides, the electrode/separator layers are rolled. As a result, the layers are perpendicular to the imaging plane at these sides, leading to a through-thickness or an inclined wave transmission of the layers. For a wave propagation from an emitter to the opposite receiver, the excited waves first propagate through the thickness direction of the layers and then along the mid-layers as straight rays. For the inclined transmission in the inhomogeneous region of the imaging plane, the wavefront can be elliptical due to the anisotropy of the stacked layers at the macro scale. This implies the wave propagation path within this area is curved. However, considering the small curvature, the limited size of the inhomogeneous region, and the low resolution required for temperature mapping, we simplify the path within this area as a direct line.
Given the mixing of through-thickness and in-plane transmission within one path, additional measure-

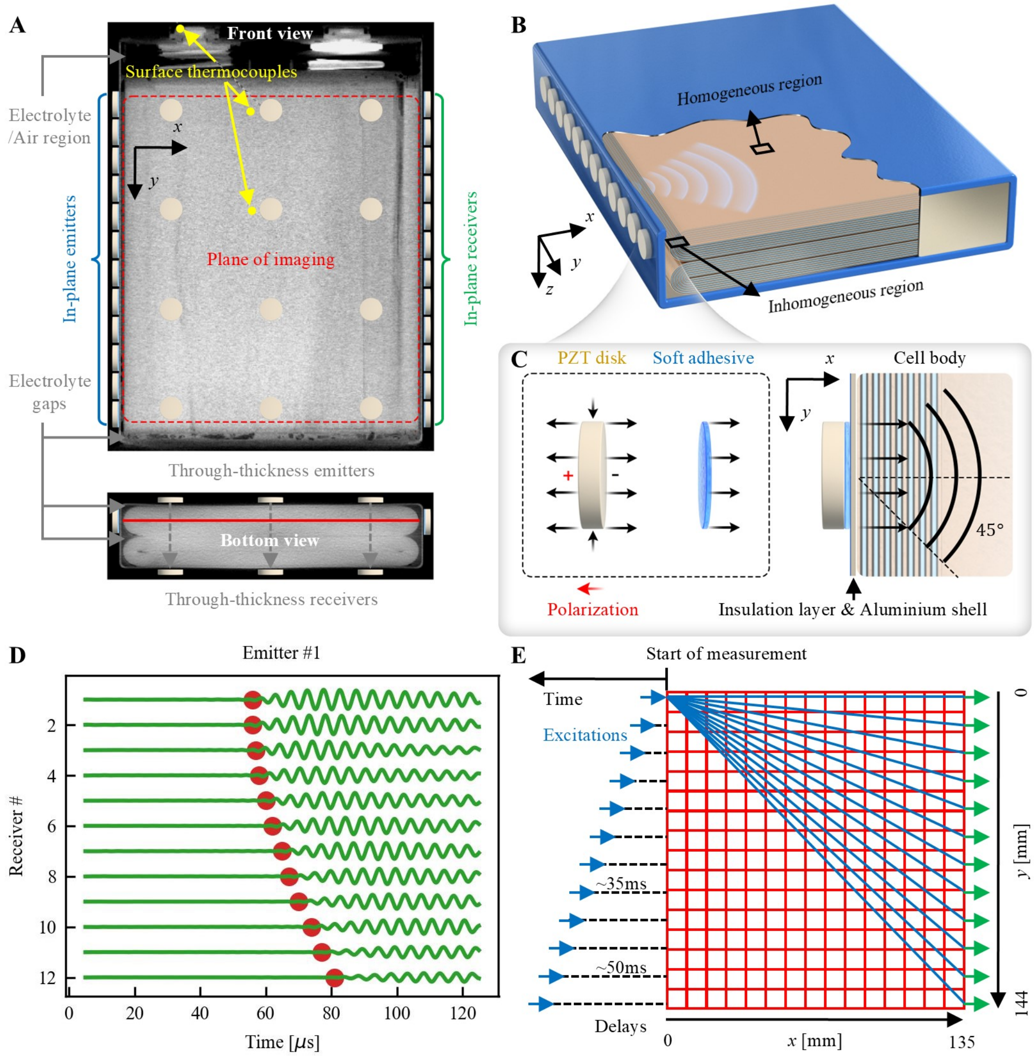

Figure 2: Configuration of ultrasound tomography for imaging internal temperatures in a prismatic cell. (A) The internal structure of the prismatic cell revealed by X-ray CT, showing two rolls of prismatically winded electrode/separator layers and electrolyte/air gaps in a rigid shell. This panel also includes a schematic of the imaging plane and the placement of ultrasonic emitters/receivers. (B) Schematic of wave propagation in the imaging plane, which contains two inhomogeneous regions at the sides and a main homogeneous region. In the inhomogeneous regions, the propagation direction is right/inclined through the thickness of the layers, while in the homogeneous region, it is along the plane of layers. (C) Soft adhesive to selectively generate and receive out-of-surface displacements. (D) Example denoised signals excited by the top emitter at 25 °C and a fully charged state with red dots indicating arrival times based on a speed of 2400 m/s. (E) Illustration of the sequential excitation order of ultrasonic waves (5 ms interval to avoid interference), wave propagation paths, and discretization of the imaging area.

ments are needed to determine their temperature effects separately. Thus, supplementary ultrasonic transducers are placed on the front and back surfaces for through-thickness transmission measurements, as shown in Figure 2A. These transducers can also provide through-thickness-averaged temperatures at their locations after temperature effect calibration, serving as cross-validation for the tomography results.

The ultrasonic emitters and receivers are PZT (lead zirconate titanate) disks, which can convert energy between vibrations and voltages. As depicted in Figure 2C, the applied or reacted electric field is parallel to the polarization direction. Consequently, both in-surface and out-of-surface displacements can be generated and sensed. However, the in-surface displacements excite strong S_0 mode Lamb waves propagating in the prismatic shell. Although the shell corners and internal leakage dampen the Lamb waves, their presence is still significant. To suppress Lamb wave interference and receive pure bulk longitudinal waves propagating internally, soft adhesives that only maintain out-of-surface displacement continuity are used to bond the PZT disks to the surface.

Figure 2D shows example denoised signals excited by the top emitter at 25 °C and a fully charged state. Each received signal contains a distinct bulk wave packet with a center frequency of 0.2 MHz. Based on the arrival times of the ultrasonic waves, indicated by the red dots in Figure 2D, the wave velocity is approximately 2400 m/s. Consequently, the wavelength is approximately 12 mm.

The height of the imaging area is limited by the emitter's beam angle range, which is approximately ±45 °. As shown in Figure 2E, the height is 144 mm, slightly smaller than the height of the electrode rolls. The center-to-center distance between two neighboring emitters/receivers is 12.7 mm, given their diameter of 10 mm. Consequently, there are 12 emitters/receivers. The emitters sequentially excite waves at approximately 5 ms intervals, ensuring the waves from the previous emitter fully dissipate and allowing each receiver to record waves from each emitter individually. The total data collection time is less than 0.1 s. This step results in 12×12 emitter-receiver signal channels, with the propagation paths covering the entire imaging area.

Given that the imaging plane is nearly homogeneous, and the temperature distribution is continuous with small gradients, the diffraction and refraction of ultrasonic waves can be neglected. This allows the propagation of ultrasonic waves from the emitter to the receiver to be approximated as straight rays. Under this approximation, travel times are treated as line integrals of local slowness (inverse of velocity) along ray paths [45, 46, 47, 48]. A slowness map can be reconstructed using a tomography process adapted from the approach used in X-ray CT-based reconstruction systems [44].

Since this is a typical limited-angle and sparse-view tomography problem, a direct solution is not feasible, necessitating the discretization of the imaging area for a numerical solution [49]. The pixel size is set to 9 mm, resulting in a grid of 16×15 pixels.

With the ultrasonic waves approximated as straight rays and the imaging area discretized, the travel times can be expressed with a linear system:

$$\mathbf{t} = W\mathbf{s}, \tag{1}$$

where $\mathbf{t} \in \mathbb{R}^{144\times1}$ includes the arrival times of 144 emitter-receiver channels, $\mathbf{s} \in \mathbb{R}^{240\times1}$ includes the slowness of all pixels, and the element $W[i, j]$ in $W \in \mathbb{R}^{144\times240}$ represents the intersection length between the i-th emitter-receiver path and the j-th pixel.

In practice, due to the noisy and weak signals, extracting accurate travel times is challenging. Instead, we use signals at 25 °C and the fully charged state as baselines and calculate the shifts in travel times $\Delta\mathbf{t}$ between the current signals and the baselines by comparing their full waveforms. The extraction of $\Delta\mathbf{t}$ is more accurate and robust than that of $\mathbf{t}$ due to the consideration of the full waveform. As a result, (1) becomes

$$\Delta\mathbf{t} = W\Delta\mathbf{s}. \tag{2}$$

Tomographic reconstruction involves solving this linear system using Algorithm 1 with the measured arrival time shifts as input. Once the slowness distribution is determined, the temperature distribution can

be derived using the correlation between slowness and temperature obtained through temperature effect calibration.
The tomographic reconstruction algorithm is highly efficient, requiring less than 0.1 s per reconstruction on a standard laptop. This efficiency, combined with streamlined data collection, enables real-time monitoring.

2.2 Temperature effect calibration

The cell equipped with the ultrasonic system was placed in a climatic chamber. To calibrate the temperature effect on ultrasonic slowness, the climatic chamber maintained a specific temperature for several hours to create a uniform temperature distribution within the battery. As a result, the shifts of travel times, $\Delta\mathbf{t}$, due to the transition from the baseline temperature (25 °C) to the current temperature can be obtained. By varying the temperature in the chamber and repeating this process, the temperature effect on slowness can be obtained.
Figure 3A presents the in-plane travel times, $\Delta\mathbf{t}_{xy}$, measured across 144 emitter-receiver channels at four different temperatures, demonstrating a clear linear correlation. The temperature effect of the in-plane travel times, $(\mathrm{d}\mathbf{t}/\mathrm{d}T)_{xy}$, is subsequently determined through linear regression on this data, as shown in Figure 3B. Similarly, the temperature effect of the through-thickness travel time, $(\mathrm{d}t/\mathrm{d}T)_{zz}$, is obtained by taking the average of the results from 12 through-thickness channels, as illustrated in Figure 3C.
The horizontal propagation from an in-plane emitter to its opposite receiver is equivalent to the sum of through-thickness transmission in the two inhomogeneous regions and in-plane transmission in the homogeneous region. The temperature effect of travel time at the inhomogeneous regions should be half of $(\mathrm{d}t/\mathrm{d}T)_{zz}$, as the total width of the inhomogeneous regions is half of the cell thickness. Thus, the temperature effect of the slowness at the homogeneous region can be expressed as:

$$\begin{aligned}(\mathrm{d}s/\mathrm{d}T)_{\mathrm{homogeneous}} &= \frac{(\mathrm{d}t/\mathrm{d}T)_{\mathrm{homogeneous}}}{w_{\mathrm{homogeneous}}} \\ &= \frac{[(\mathrm{d}t/\mathrm{d}T)_{xx} - (\mathrm{d}t/\mathrm{d}T)_{zz}/2]}{w_{\mathrm{homogeneous}}},\end{aligned} \tag{3}$$

where $(\mathrm{d}t/\mathrm{d}T)_{xx}$ represents the average of temperature effects for the 12 horizontal (x-direction) propagation channels and $w_{\mathrm{homogeneous}}$ is the width of the homogeneous region.
As $(\mathrm{d}s/\mathrm{d}T)_{\mathrm{homogeneous}}$ is identical at different directions within the imaging plane, we can use it to derive the temperature effects in the inhomogeneous regions for any transmission directions, $(\mathrm{d}\mathbf{s}/\mathrm{d}T)_{\mathrm{inhomogeneous}} \in \mathbb{R}^{144\times 1}$, as follows:

$$(\mathrm{d}\mathbf{s}/\mathrm{d}T)_{\mathrm{inhomogeneous}} = \frac{(\mathrm{d}\mathbf{t}/\mathrm{d}T)_{xy} - (\mathrm{d}s/\mathrm{d}T)_{\mathrm{homogeneous}}\,\mathbf{l}_{\mathrm{homogeneous}}}{\mathbf{l}_{\mathrm{inhomogeneous}}}, \tag{4}$$

where $\mathbf{l}_{\mathrm{homogeneous}} \in \mathbb{R}^{144\times 1}$ and $\mathbf{l}_{\mathrm{inhomogeneous}} \in \mathbb{R}^{144\times 1}$ include the propagation lengths of 144 emitter-receiver channels in the homogeneous region and the inhomogeneous regions, respectively.
The results are visualized in Figure 3D. The angle represents the propagation angle with the x-axis (horizontal). We can observe that, the temperature effect in the inhomogeneous region is several times larger than that in the homogeneous region. Additionally, this difference diminishes as the angle approaches 90 °, which is equivalent to homogeneous propagation.
The significant difference between homogeneous and inhomogeneous temperature effects can create spatial discontinuities in $\Delta\mathbf{s}$, which is not ideal for the tomographic reconstruction algorithm. To ensure the continuity of $\Delta\mathbf{s}$, scaling factors $\alpha = \frac{(\mathrm{d}\mathbf{s}/\mathrm{d}T)_{\mathrm{inhomogeneous}}}{(\mathrm{d}s/\mathrm{d}T)_{\mathrm{homogeneous}}}$ are applied to the elements in W corresponding to pixels intercepting with the inhomogeneous regions.

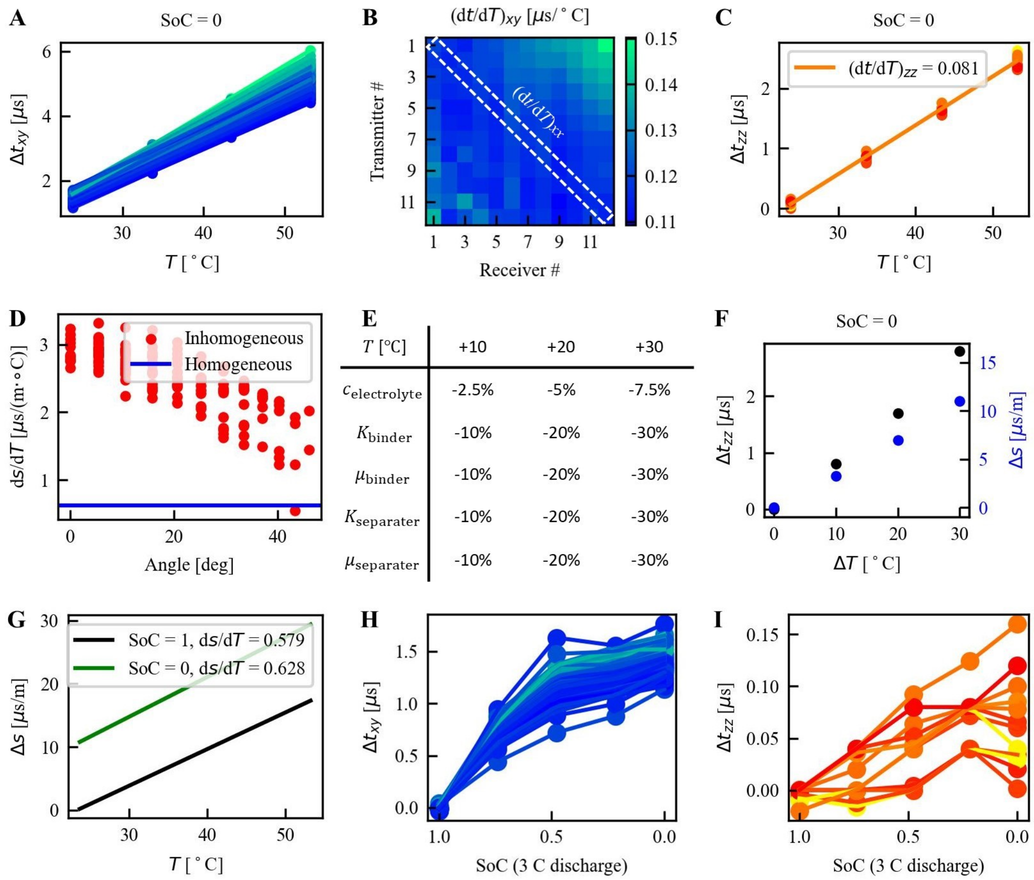

Figure 3: Temperature effect calibration and simulation, and SoC effect at 25 °C.(A) Evolution of travel time of each in-plane channel t_{xy} with temperature. (B) Temperature effect $(\mathrm{d}t/\mathrm{d}T)_{xy}$ of the in-plane channels obtained by linear fitting. The diagonal values correspond to the temperature effect for horizontal transmissions, $(\mathrm{d}t/\mathrm{d}T)_{xx}$. (C) Evolution of travel time of each through-thickness channel t_{zz} with temperature and the temperature effect $(\mathrm{d}t/\mathrm{dT})_{zz}$ obtained by linear fitting and channel-wise averaging. (D) Temperature effect of the slowness of each in-plane channel in the inhomogeneous regions, $(\mathrm{d}s/\mathrm{d}T)_{\text{inhomogeneous}}$, and the temperature effect in the homogeneous region, $(\mathrm{d}s/\mathrm{d}T)_{\text{homogeneous}}$. The horizontal axis represents the propagation angle relative to the x-direction for in-plane channels. (E) The temperature-dependent input parameters for temperature effect simulation. (F) Temperature effects of through-thickness travel time and slowness in the homogeneous region by simulation. (G) The temperature effects of slowness in the homogeneous region at different SoCs. (H and I) The SoC effect on travel time for (H) in-plane channels and (I) through-thickness channels. The measurements were taken after the cell had sufficiently rested following partial 3 C discharges.

2.3 Explanation for the temperature effect by simulation

The temperature effect is primarily attributed to the temperature dependence of material properties, including the stiffness of solids, the sound speed of fluid, and the thermal expansion. The thermal expansion is typically very small, with a relative size change on the order of 10^{-5} per unit change in temperature, which can be neglected. The change in stiffness of crystalline materials (Al, Cu, Graphite, and $LiFePO_4$) is also small, typically on the order of 10^{-4} in relative change [50, 51]. In contrast, the stiffness of plastics (binders and separators) is more sensitive to temperature, with changes on the order of 10^{-2} [52, 53]. Moreover, the relative change in sound speed in electrolytes is about 2.5×10^{-3} [54]. A quasi-1-D through-thickness wave propagation model was used to evaluate the effects of these parameter changes, as listed in Figure 3E, on the through-thickness travel time. The results, listed in Figure 3F, show that the simulated travel time has a linear correlation with temperature, with a coefficient of 0.093 μs/°C, which is close to the experimental value shown in Figure 3C.

Additionally, a quasi-1-D numerical model for wave propagation along the layers was established. Consequently, we have a simulated $(\mathrm{d}s/\mathrm{d}T)_{\text{homogeneous}}$ of 0.368 μs/(m·°C), as shown in Figure 3F, which is 59% of the experimental value in Figure 3D.

In summary, the temperature effect is primarily attributed to the temperature-dependent mechanical properties, including the electrolyte sound speed and the stiffness of the binder and separator.

2.4 SoC effect compensation

In addition to temperature effects, the travel time of ultrasonic waves within the imaging plane is also sensitive to the state of charge (SoC). As shown in Figure 3G, there is a noticeable offset between the slownesses at SoC = 0 and SoC = 1. Therefore, decoupling the effects of SoC and temperature is crucial for operando temperature imaging. Fortunately, simulations show that the key temperature-dependent parameters are uncorrelated with SoC, indicating that the temperature effect on travel time is independent of the SoC effect. This assumption is supported by experimental findings from the literature [40, 41] and the results in Figure 3G, where the temperature effect on slowness, $\mathrm{d}s/\mathrm{d}T$, remains almost constant (7.8% difference) across different SoC levels. As a result, the total shift in slowness/travel time can be approximated as the superposition of temperature-induced and SoC-induced shifts, and the SoC effect can be compensated in real-time through direct subtraction.

The SoC effect was pre-determined through partial charge/discharge experiments. Since temperature and SoC effects are independent, determining the SoC effect at a single temperature is sufficient. After each quarter-cycle of charging or discharging, a resting phase allowed the battery to stabilize thermally and returned to room temperature (25 °C). The travel time corresponding to the current SoC was then recorded. By repeating this process, a relationship between SoC and travel time was established, as shown in Figures 3H and 3I. The results indicate that while through-thickness travel time is relatively insensitive to SoC, in-plane travel time shows significant sensitivity to SoC. Using this pre-determined correlation and the SoC provided by coulombic counting, the travel time during a full discharge at 3 C can be compensated for SoC effects in real-time.

2.5 Temperature monitoring under external heat

In practice, active thermal management with external heating or cooling sources is applied to keep batteries within an optimal thermal range. Additionally, unexpected external heat sources can potentially trigger thermal runaway, making it crucial to evaluate the thermal performance of batteries subjected to external heat.

In this study, a small heat plate was attached to the bottom surface at the bottom right corner of the battery. The temperature evolution with continuous heating at 50 °C is shown in Figure 4. The internal temperature gradually increased from the bottom right corner, reaching a maximum of 31.6 °C after 27 minutes, which is 4.2 °C higher than the ambient temperature. The overall efficiency of heat conduction was not particularly high.

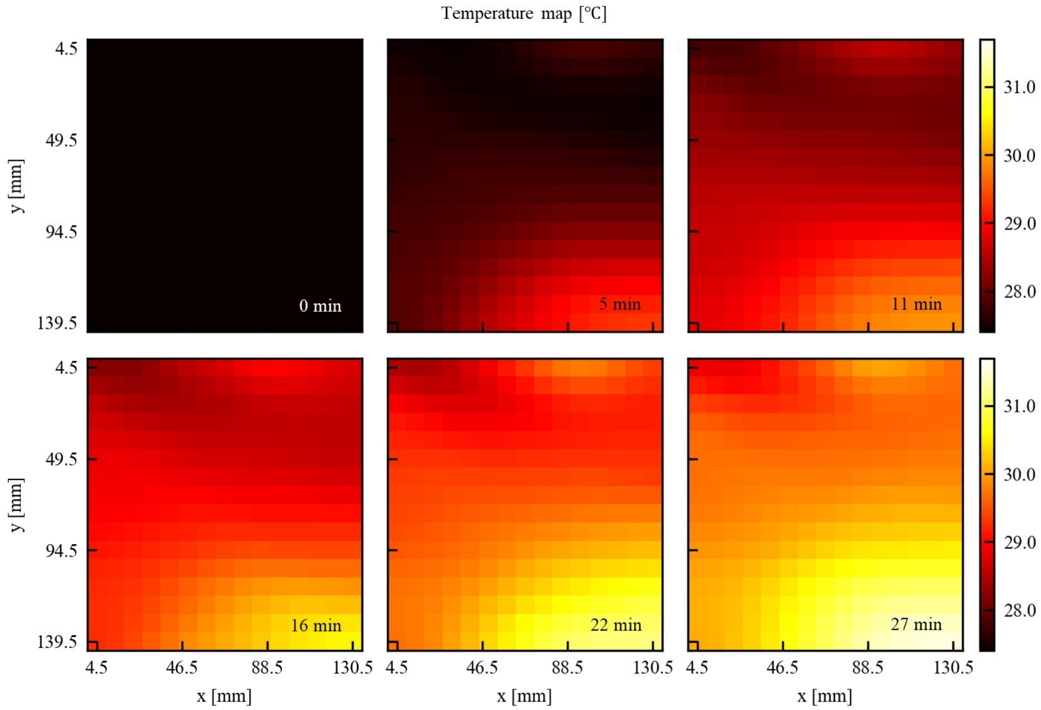

Figure 4: The internal temperature distributions subjected to a 50 °C external heat source located at the bottom right corner. The video showcasing the experimental setup and real-time temperature mapping is shown in Movie S1.

To validate the temperatures provided by the tomography algorithm, the thickness-averaged temperatures obtained through the temperature effect calibration of the through-thickness travel times at 12 positions (as depicted in Figure 2A) are used as a reference. The internal temperatures over time at these 12 positions are plotted in Figure 5, alongside the thickness-averaged temperatures. Although the averaged temperatures show some rounding errors due to the ultrasonic signal sampling frequency, the internal and average temperatures are close at most positions, indicating that the tomography algorithm is well-validated.
At positions farther from the heat source, the internal temperature tends to be higher than the average temperature. This is reasonable because heat convection at the surface dominates at these locations, leading to a thermal gradient in the thickness direction.

2.6 Temperature monitoring during fast discharging

In practice, the most demanding conditions for a cell occur during full charges or discharges at high rates. Given that the maximum charge/discharge rate of the prismatic cell is 3 C and the highest operating temperature is 55 °C, the cell's thermal performance was evaluated during a full discharge at 3 C, with an ambient temperature maintained at 25 °C by a chamber.
Each minute, the SoC-compensated travel time shifts were processed using Algorithm 1, and the resulting slowness map was converted into a temperature map based on the temperature effect calibration. Figure 6 displays snapshots of the internal temperature distribution during a full discharge at a 3 C rate. A vertical thermal gradient emerges early in the discharge, with a higher temperature region consistently near the poles. By the end of the discharge, the maximum temperature reaches 46.3 °C, which is 22.5 °C above ambient temperature. At any given moment, the temperature difference can be as much as 8 °C, underscoring the importance of temperature mapping. This thermal inhomogeneity is attributed to current concentration and heat generation near the poles.
The internal temperatures at the 12 through-thickness measurement positions were extracted for further analysis in the time domain and compared with temperatures measured by other tools. As shown in Figure 7, during the fast discharge, the temperature increase rate exhibited three distinct stages: fast, slow,

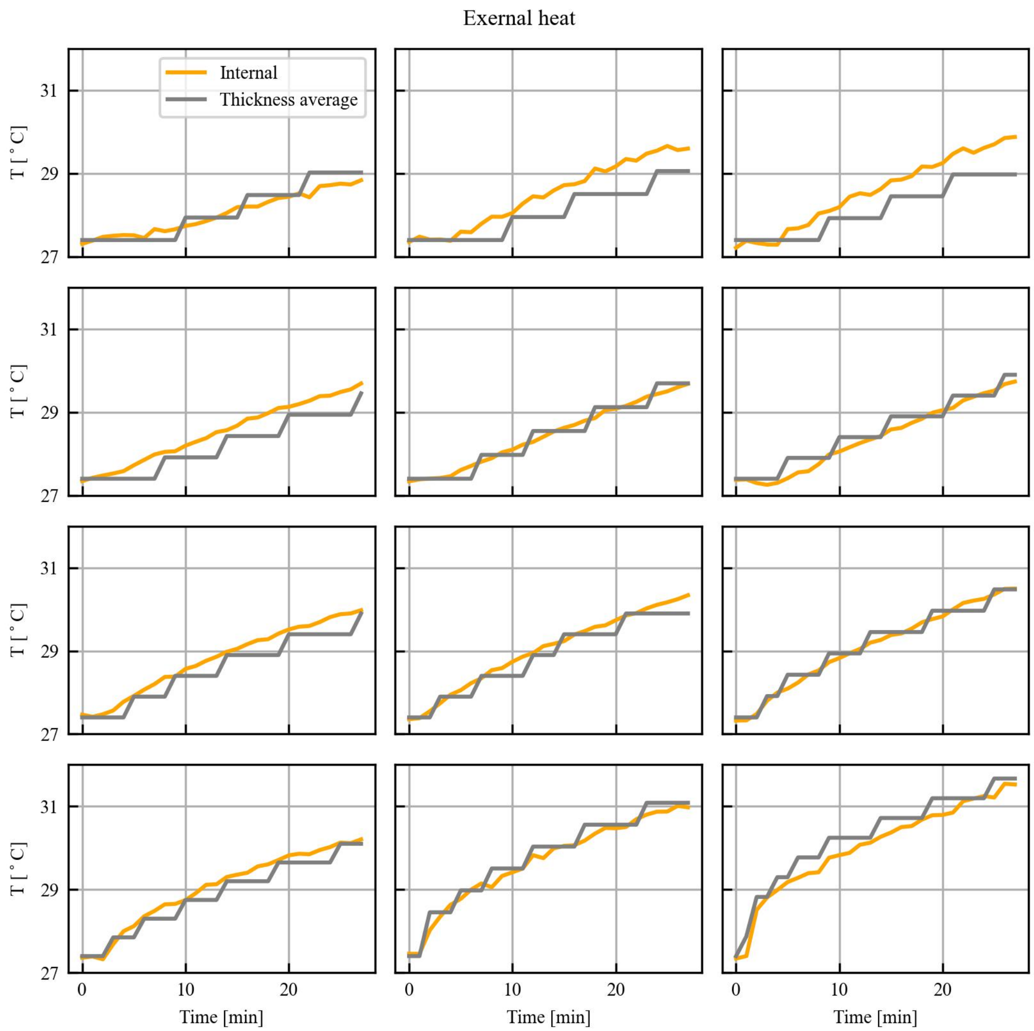

Figure 5: Local temperature evolution over time at the 12 through-thickness measurement positions depicted in Figure 2A, subjected to a 50 °C external heat source located at the bottom right corner. Each subfigure plots the temperature at a single position, with the subfigures arranged to correspond to their actual relative positions.

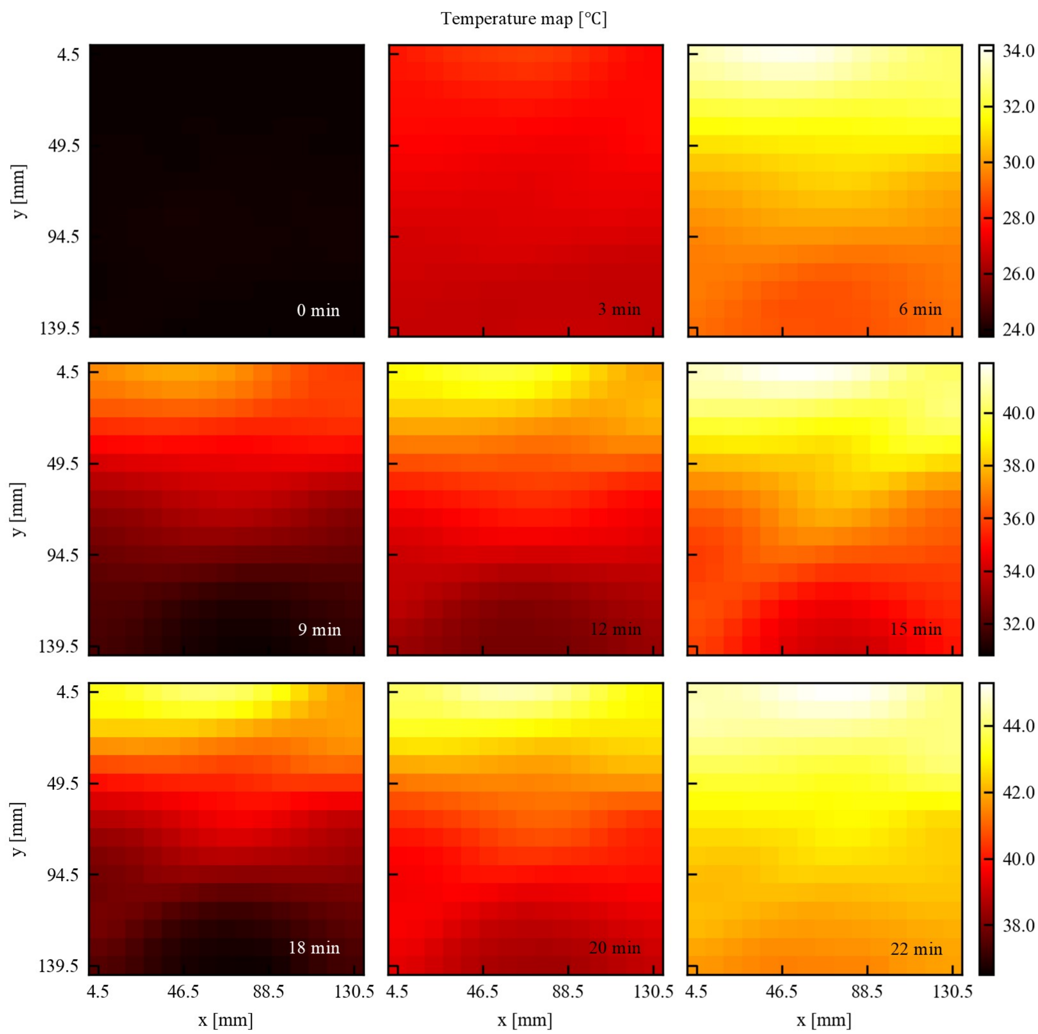

Figure 6: The internal temperature distributions during a full discharge at 3 C. The animated version of the temperature evolution is Movie S6.

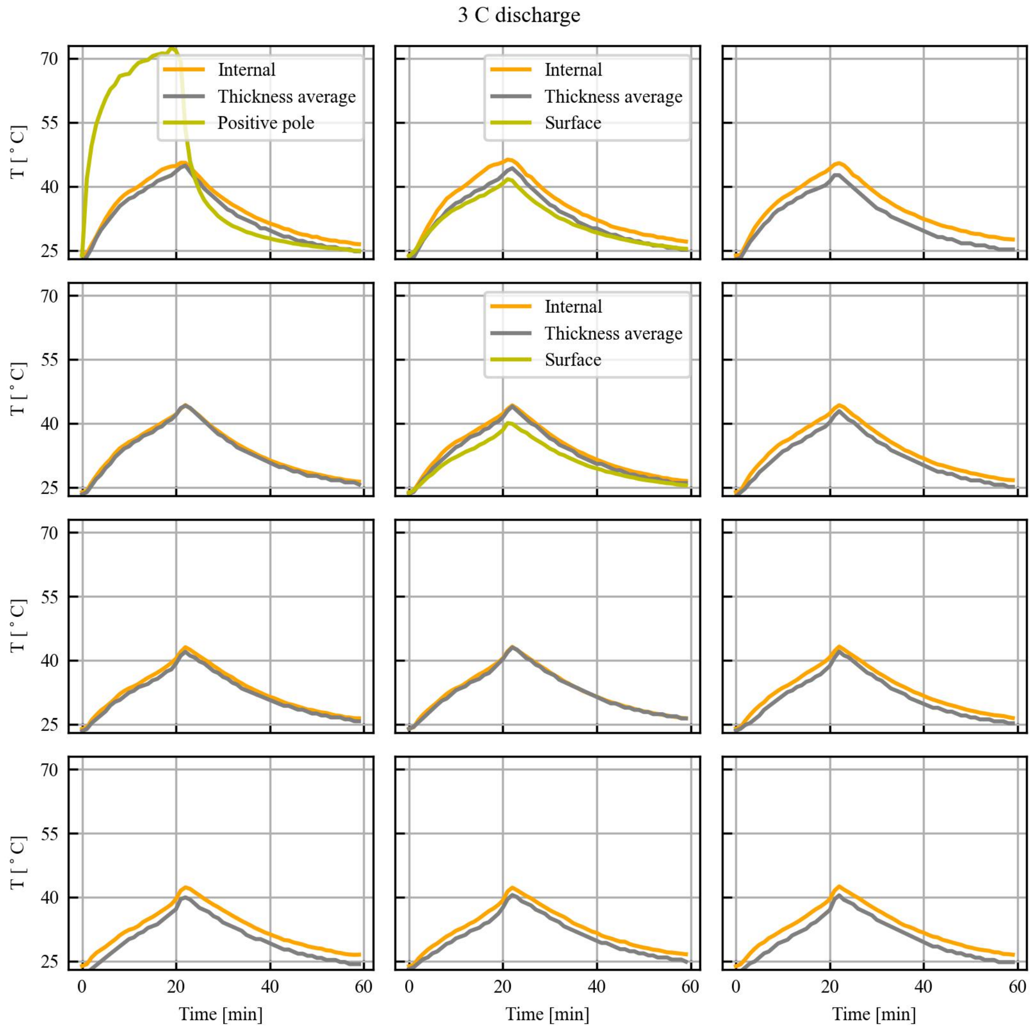

Figure 7: Local temperature evolution over time at the 12 through-thickness measurement positions depicted in Figure 2A during a full discharge at 3 C and the subsequent resting stage. Each subfigure plots the temperature at a single position, with the subfigures arranged to correspond to their actual relative positions.

and then fast again, consistent with simulations and experiments reported in the literature [20, 21, 22, 24, 27, 32]. During the subsequent resting stage, the overall temperature gradually decreases, and the thermal inhomogeneity diminishes.

The average temperature across the thickness, as measured by the through-thickness transducers, follows the same trend as the internal temperature at one-quarter thickness. However, the average temperature is consistently lower than the internal temperature, particularly in the top region. This similarity in the evolution pattern validates the internal temperature reconstruction obtained through tomography. Meanwhile, the observed bias between internal and average values confirms the presence of temperature inhomogeneity along the thickness direction.

Surface temperatures measured by two type-K thermocouples at the positions shown in Figure 2A also follow a similar pattern to the internal and average temperatures at those positions. However, these surface temperatures are consistently the lowest, which is expected. The maximum difference between internal and surface temperatures can be as much as 5.9 °C. In contrast, the temperature at the positive pole is significantly higher than the other measured temperatures, reaching up to 73 °C. This observation aligns with the findings of previous experiments [22, 24, 25], indicating substantial heat generation at the battery poles and tabs, contributing to the high-temperature regions near these components.

3 Discussion

3.1 Integration into an electric vehicle and cost analysis

The current system employs PZT disks with a thickness of 2 mm and manually assembled wiring. However, space constraints in electric vehicles necessitate a more compact solution. This can be addressed by using customized sensor films[2], in which sub-millimeter-thick PZT disks, wiring, adhesives, and shielding are fully integrated. The total thickness of these films can be less than 1 mm, allowing them to be easily mounted on the side surfaces of battery cells.
Although each cell requires two sensor arrays, the entire vehicle can be equipped with a single multi-channel ultrasonic controller. This is feasible because the data acquisition for each diagnosis takes less than 0.1 seconds. If diagnostics are performed at one-minute intervals, a 24-channel controller can serve up to 600 cells, which is sufficient for a typical electric vehicle.
The controller used in our experiments is a general-purpose 64-channel unit with dimensions of 120 mm × 280 mm × 310 mm and a weight of less than 5 kg. For integration into electric vehicles, a custom-designed 24-channel controller could be used, with the size and weight potentially reduced by at least half. Thanks to the system's compact and lightweight design, integration is unlikely to pose a challenge. The system is also energy-efficient, with the current controller operating at just 50 W. This makes the system well-suited to function as a sub-module within the battery management system (BMS), delivering accurate internal temperature data to support advanced thermal management strategies.
Regarding cost, the sensors and wiring per cell are estimated at approximately USD 10. The controller costs around USD 1,000. For a battery pack with 200 cells, the total system cost would be approximately USD 3,000. This cost could be further reduced through large-scale manufacturing.

3.2 Working temperature range

The working temperature range of the system is primarily determined by the properties of the PZT disks and the adhesives used. Typically, PZT materials operate reliably within a range of approximately –40 °C to 150 °C. The selected adhesive also withstands prolonged exposure to temperatures up to 149 °C. Given that the goal of this system is not to monitor thermal runaway events directly but to provide early detection and prevent their onset, this temperature range is sufficient for the intended application.

3.3 Adaptability to other cell types

The proposed technology does not impose strict limitations on cell size. The primary requirement is that the aspect ratio (height-to-width) should not be too small to avoid severe limited-angle artifacts in tomographic reconstruction.
This approach can also be readily adapted to pouch cells. In such cases, transducers can be bonded to the main surface, and guided waves can be employed for temperature mapping. The key requirement is that the wave propagation occurs along the homogeneous planar layers of the cell. Consequently, this technique is not applicable to cylindrical cells due to their curved geometry and inhomogeneous propagation path.
The method is also compatible with cells of different chemistries. This is because the temperature dependence of the measured wave velocity is primarily governed by the temperature-sensitive properties of components such as binders, separators, and electrolyte—materials that are largely independent of the specific cell chemistry.

3.4 Potential SoC compensation error at high C-rates

One potential concern is that during fast charging or discharging, the SoC effect may deviate from the pre-established SoC–ultrasonic travel time correlation measured at equilibrium. This deviation arises from dynamic effects caused by lagged lithium-ion diffusion, which could introduce compensation errors.

[2] See example at https://www.acellent.com/products/smart-layer-sensors

Fortunately, we did not observe abrupt changes in ultrasonic travel time at the onset or termination of large currents—a behavior typically seen in voltage responses under dynamic conditions. However, some hysteresis or relaxation in ultrasonic travel time may still exist due to delayed lithium diffusion. The challenge is that these effects cannot be easily separated from the temperature contribution, making it difficult to quantify them directly.

In future work, we plan to employ advanced cross-validation methods—such as embedding thermal sensors within cells—to better characterize and quantify the error introduced by dynamic SoC-related variations in ultrasonic travel time during high C-rate operations.

3.5 Stability

During electric vehicle operation, cell conditions may vary. Battery degradation, in particular, can influence ultrasonic travel time—the core parameter for temperature mapping—necessitating periodic recalibration to maintain accuracy over time.

Mechanical vibrations and occasional impacts are not expected to affect performance unless they cause significant structural damage to the cell. This is because such disturbances typically occur at low frequencies, whereas our method operates at ultrasonic frequencies and is inherently resistant to low-frequency noise.

The durability of the system itself must also be considered. Ultrasonic sensors generally have a longer lifespan than the batteries they monitor. Although adhesive aging may occur over time, commercially available adhesives with extended service lifespans can be used to ensure long-term reliability.

4 Conclusion

This paper presents a groundbreaking technology enabling non-destructive, in-situ, and real-time imaging of internal temperatures within a prismatic cell. This was achieved through the development of an ultrasound tomography imaging system, which addresses the limited-angle challenge for tomographic reconstruction using smoothing regularization (see Section 5). A temperature effect calibration method was developed, enabling the conversion of the reconstructed slowness map into a temperature map. The temperature effect was further validated through precise simulations, confirming the independence of the temperature and SoC effects on ultrasound travel time. Consequently, operando temperature mapping can be achieved with straightforward SoC effect compensation. The technology has been systematically validated using synthetic data (see Figure 9), surface thermocouples, and thickness-average measurements.

Through case studies involving external heating and fast discharging, the internal temperature distribution under realistic operational conditions was imaged for the first time. The external heating case reveals that the heat conduction efficiency is limited in prismatic cells, emphasizing the need for internal temperature monitoring to maintain the thermal state within an optimal range and detect anomalies early. During full and fast discharge, the thermal gradients of up to 8 °C were observed within the imaging plane and 5.9 °C in the cell-thickness direction, underscoring the importance of internal temperature mapping.

For larger and thicker prismatic cells, the overall heat conductivity may be lower, leading to even higher internal temperatures and greater thermal gradients. As an example, Movie S7 includes the temperature evolution of a larger but otherwise identical prismatic cell with a rated capacity of 105 Ah. During a 0.5 C discharge, the maximum temperature approaches that of the 50 Ah cell at a 2 C discharge rate.

Thanks to its compact, low-power, and cost-effective design, this ultrasonic imaging system serves as a real-time feedback mechanism for online thermal management in electric vehicle battery packs. By continuously monitoring internal temperatures, it helps maintain an optimal thermal range throughout the cell, representing a significant breakthrough in enhancing electric vehicle performance. The system is also critical for the early detection of internal thermal anomalies during abnormal events, such as internal short circuits or mechanical abuse, enabling prompt intervention to prevent further damage. For

example, Movie S4 illustrates an abnormal 2 C discharge scenario, where a 7 °C rise in internal temperature—caused by poor contact at the negative pole—is monitored in real-time. This shift from reactive detection to preventive monitoring marks a significant advancement for the safety of electric vehicles and large-scale energy storage systems.
Moreover, this technology has valuable applications as an offline testing tool for verifying battery thermal properties and designs, as well as for quality control of new cells, contributing to safer, more reliable batteries.
Currently, the system is limited to monitoring temperatures at one-quarter thickness due to the presence of corner gaps within the cell. This limitation can be addressed by modifying the cell structure to use stacked electrode layers or by improving the efficiency of ultrasonic transducers. The industry trend toward stacked electrode layers in prismatic cells, rather than rolled layers, reduces corner gap areas, enhancing the effectiveness of this technology.
In the future, errors arising from temperature effect calibration, SoC effect compensation, and the limited range of projection angles should be quantified using additional measurement tools, such as embedded thermal sensors.

5 Methods

Experiments:
PZT-5 disks with dimensions of Φ10 mm × 2 mm are used as ultrasonic emitters and receivers. These disks are polarized in the thickness direction (2 mm), with the positive electrode coated on the top surface and the negative electrode on the bottom surface. Upon application of a voltage, the disks exhibit both radial and out-of-plane displacements. The natural frequency of the disks is 200 kHz. The bottom surface of each disk is bonded to the cell surface to facilitate wave transmission. For ease of wiring, the negative electrode is equipped with an extra tab that extends to the top surface. The adhesive used for bonding is the 3M 468MP double-sided adhesive with a thickness of 0.13 mm.
The MicroPulse LTPA from Peak NDT[3] was used for generating and receiving electronic signals. A negative pulse with an amplitude of 70 V and a width of 500 ns was generated for each excitation. Although the actual signal deviates slightly from the ideal due to the characteristics of the firing circuit and the PZT disk, it still maintains a wide bandwidth. On the receiving side, a 65 dB gain and a wide-bandwidth filter were applied to the received signal. However, due to signal attenuation within the battery and the resonance of the PZT disks, the received signal is narrow-bandwidth, centered at 200 kHz. The sampling frequency was set to 25 MHz, which is sufficient to capture minimal travel time shifts as small as 0.04 μs.
Data collection for the in-plane transducers was performed in full-matrix capture (FMC) mode, where each emitter is sequentially excited while all receivers are active after each excitation. The interval between two excitations was set to more than 1 ms to prevent interference. For the through-thickness PZT transducers, the pitch-catch mode was employed, meaning the waves generated by one transducer were collected only by its directly opposite counterpart. The total time required for each data collection was less than 1 second.
For each diagnosis, data collection was repeated 16 times consecutively to allow for further signal averaging. The total time required for this process was less than 10 seconds, during which the temperature could be considered constant. Diagnoses were performed at 1-minute intervals.
Throughout the investigation of fast discharging, the battery equipped with ultrasonic transducers and connected to the battery tester was put in a climatic test chamber, which controls the ambient temperature. The battery tester used for charging/discharging the battery and recording the voltage and current was from Digatron firing circuits (Model: MCT 200-06-6 ME S). The complete experimental setup is depicted in Figure 8.

Signal processing:

[3] https://www.peakndt.com/products/micropulse-ltpa/

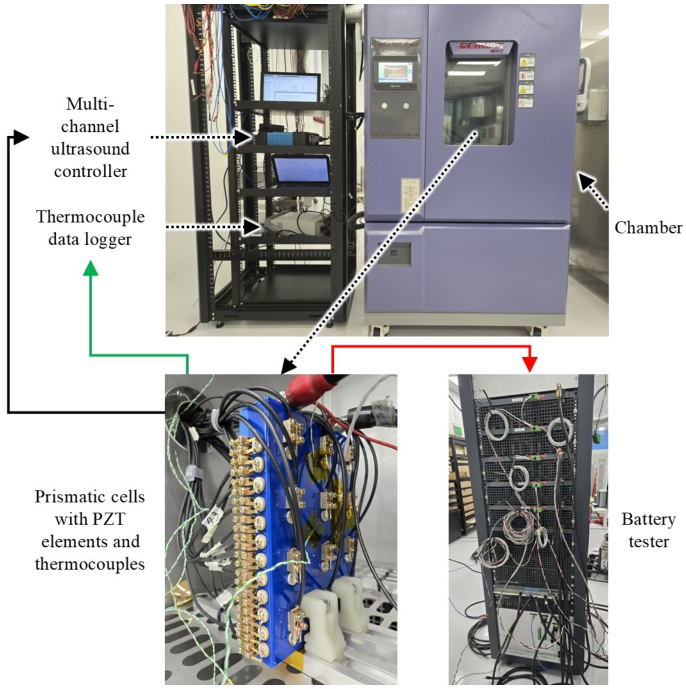

Figure 8: Operando experiment setup.

The collected data for each diagnosis can be represented by a matrix $D \in \mathbb{R}^{m \times n}$, where m represents the number of channels, and n denotes the number of sampling points in the time domain.
Next, the singular value decomposition (SVD) [55] was applied to the data matrix D to eliminate the electromagnetic interference. The rationale is that electromagnetic interference typically exhibits a distinct pattern and lower energy compared to ultrasonic signals. Consequently, both electromagnetic interference and ultrasonic signals can be represented as linear combinations of different linearly independent components, with the interference components having lower energy. The interference can be effectively removed by setting the smaller singular values, which represent the energy of the interference, to zero. Mathematically, this process is described by:

$$D = USV^{\mathrm{T}}, \tag{5}$$

where $U \in \mathbb{R}^{m \times m}$ and $V \in \mathbb{R}^{n \times n}$ are unitary matrices with rows consisting of linearly independent eigenvectors of DD^{T} and $D^{\mathrm{T}}D$ (where T represents the transpose), and $S \in \mathbb{R}^{m \times n}$ is a rectangular diagonal matrix containing non-negative singular values.
To remove the electromagnetic interference, the largest 50 singular values were preserved, while the rest were set to zero, resulting in a modified matrix S_0. The denoised data matrix $\hat{D}$ was then reconstructed as:

$$\hat{D} = US_0V^{\mathrm{T}}. \tag{6}$$

Following SVD denoising, a fast Fourier transform (FFT) was applied for each time-domain signal to further reduce high-frequency noise. Both SVD and FFT denoising were implemented using NumPy in Python.
With the denoised data, the change in travel time $\mathbf{\Delta t}$ is determined using the Pearson correlation coefficient (PCC). The shift in signals that maximizes the PCC between the current data and baseline measurements is identified as $\mathbf{\Delta t}$.
In practice, since temperature changes slowly, resulting in continuous travel time changes, the extraction of $\mathbf{\Delta t}$ will refer to the value extracted during the previous diagnosis (one minute prior). This approach limits the search range to a small, localized area near the previous value, thereby avoiding cycle-skipping under low signal-to-noise ratio (SNR) conditions. Notably, channels with very low SNR were classified as dead channels to prevent their negative impact on the results.

Tomographic reconstruction:
For limited-angle tomography, iterative reconstruction methods are preferred over filtered back projection (FBP) [49]. In this study, we use the simultaneous iterative reconstruction technique (SIRT), which is well-suited for limited-angle problems and offers robustness against noise [49, 56]. At the k-th iteration, the reconstruction update is given by [57]

$$\Delta\mathbf{s}^{(k)} = \Delta\mathbf{s}^{(k-1)} - CW^{\mathrm{T}}R\left(W\Delta\mathbf{s}^{(k-1)} - \Delta\mathbf{t}\right), \tag{7}$$

where C and R are diagonal matrices with elements $C[j,j] = 1/\sum_i W[i,j]$ and $R[i,i] = 1/\sum_j W[i,j]$. This update integrates corrections from all channels, providing better noise artifact suppression compared to the basic algebraic reconstruction technique (ART).
The limited-angle problem introduces ill-posedness into the reconstruction process due to insufficient data. To address this, additional prior knowledge should be incorporated as a regularization term [58]. Given the continuous nature of the temperature distribution and its small gradients, we employed the smoothing regularization (Tikhonov regularization) [59, 60, 61]. This was achieved using a Gaussian filter from SciPy in Python. A 2-D Gaussian kernel G was used for convolution on the reconstructed slowness map, represented by

$$G[i,j] = \frac{e^{-0.5\left(i^2+j^2\right)}}{\sum_{a=-4}^{4}\sum_{b=-4}^{4} G[a,b]}, \tag{8}$$

where $i \in [-4,4]$ and $j \in [-4,4]$. The slowness map was first reshaped from a 1-D vector $\Delta\mathbf{s} \in \mathbb{R}^{240\times1}$ to a 2-D matrix $\Delta S \in \mathbb{R}^{16\times15}$ before the convolution operation and then reshaped back to a 1-D vector after the operation.
The regularization and reconstruction processes are alternated [62, 63], where each iteration of (7) is followed by a smoothing operation. Initialization is either zero or the previous tomography result $\Delta\mathbf{s}_0$, as the temperature distribution changes continuously over time. The iteration process concludes when the fitting error ϵ no longer decreases or the maximum number of iterations, set at 100, is reached. The entire algorithm is summarized in Algorithm 1.

Algorithm 1 Iterative tomographic reconstruction with smoothing regularization

Require: $\Delta\mathbf{t}$ and W
Ensure: $\Delta\mathbf{t} = W\Delta\mathbf{s}$
$\Delta\mathbf{s}^{(0)} \leftarrow \mathbf{0}$ or $\Delta\mathbf{s}_0$
$k \leftarrow 1$
$\epsilon_0 \leftarrow \|W\Delta\mathbf{s}^{(0)} - \Delta\mathbf{t}\|_2$
while $k \leq 100$ **do**
  $\Delta\mathbf{s}^{(k)} \leftarrow \Delta\mathbf{s}^{(k-1)} - CW^{\mathrm{T}}R\left(W\Delta\mathbf{s}^{(k-1)} - \Delta\mathbf{t}\right)$
  $\epsilon \leftarrow \|W\Delta\mathbf{s}^{(k)} - \Delta\mathbf{t}\|_2$
  if $\epsilon \geq \epsilon_0$ **then**
    break
  end if
  $\epsilon_0 \leftarrow \epsilon$
  $\Delta\mathbf{s}^{(k)} \rightarrow \Delta S^{(k)}$
  $\Delta S^{(k)}[m,n] \leftarrow \sum_{i=-4}^{4}\sum_{j=-4}^{4} \Delta S^{(k)}[m+i,n+j]G[i,j]$
  $\Delta S^{(k)} \rightarrow \Delta\mathbf{s}^{(k)}$
  $k \leftarrow k+1$
end while
  return $\Delta\mathbf{s}^{(k)}$

Algorithm 1 was initially demonstrated using synthetic travel time data generated from (1), based on an arbitrary velocity map designed to mimic real conditions. Random noise following a Gaussian distribution with a standard deviation of 0.17 μs, comparable to the noise level observed in experiments, was added to the synthetic travel times.

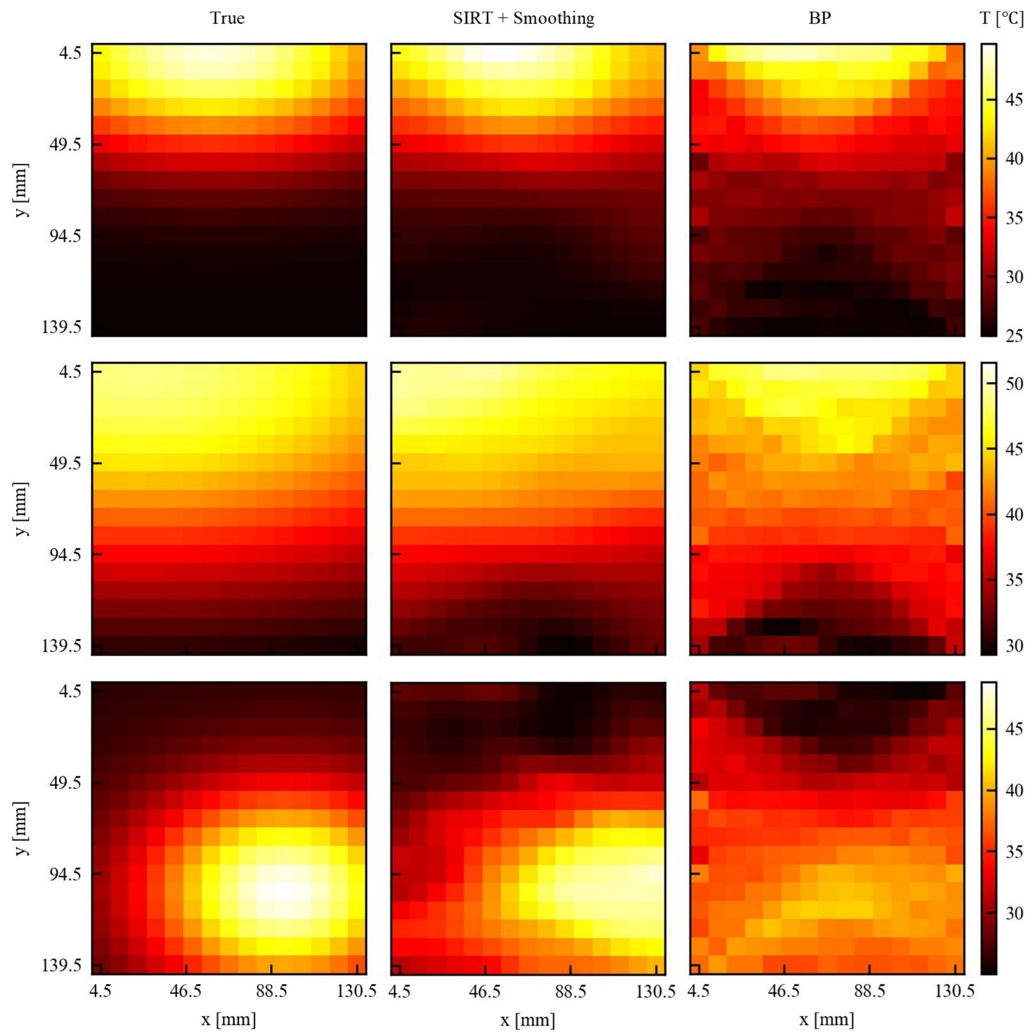

Figure 9: True and reconstructed temperature maps from three simulated cases using different algorithms.

Each true temperature map shown in Figure 9 features a high-temperature region with a Gaussian distribution, differing in position and size. The first two cases simulate localized heating caused by fast charging or discharging, while the third case represents a high-temperature region induced by an internal short circuit.
The proposed algorithm (SIRT + Smoothing) successfully reconstructs temperature maps that closely resemble the true distributions. The mean absolute errors (MAEs) for the three cases are 0.53 °C, 0.57 °C, and 1.53 °C, respectively—indicating an acceptable level of accuracy. In comparison, the basic back-projection (BP) method yields significantly higher errors of 1.86 °C, 1.54 °C, and 3.60 °C, likely due to limited projection angles and noise. These results highlight the proposed algorithm's effectiveness in addressing the challenges of limited-angle tomography and measurement noise.

Acoustic simulation:
The internal structure of the prismatic cell consists of stacked layers. Among these layers, the current collectors (made of Cu and Al) are simple linear elastic solids. The separator, however, is a fluid-saturated porous material, with its solid phase consisting of polypropylene (PP) and a fluid phase of electrolyte. Both the anode and cathode are also porous, with their solid phase comprising several materials listed in Table 1, along with an electrolyte fluid phase. The complexity of simulating wave propagation in batteries and the effect of temperature on travel time arises primarily from the multi-layer structure and the porous microstructures of the electrode and separator layers.
The electrodes consist of multiple solid materials, making an analytical solution based on Biot theory [64], which assumes a homogeneous solid phase, impractical for this case. To accurately model sound

Table 1: Material weight fraction of the prismatic cell

	Material	Weight[a]
Cathode solid phase	$LiFePO_4$	30.1%
	PVDF	0.8%
	Carbon black	1.3%
Anode solid phase	Graphite	16.5%
	CMC	0.4%
	SBR	0.4%
	Carbon black	0.2%
	Al	17.5%
	Cu	9.7%
	PP	1.9%
	Electrolyte	21.3%

[a] Sources: https://www.evebattery.com/ and https://www.mtixtl.com/.

speed across these porous layers, a 3-D numerical model that accounts for micro-scale fluid-solid interactions is necessary [65]. To model wave transmission in both the through-thickness and in-plane directions of the cell, it is crucial to account for the multi-layered structure. In the in-plane direction, wave velocity is influenced by the coupling between different layers, while in the through-thickness direction, multi-reflections at interfaces impact wave travel time. Given the need for such a large-scale model, the finite-difference time-domain (FDTD) method is ideal due to its computational efficiency compared to other numerical methods.

For modeling wave propagation in both fluid and solid media, a velocity-stress formulation can be adopted in FDTD, which describes dynamics in both media. This formulation implicitly handles the fluid-solid interaction between different materials [66]. Material changes and heterogeneities are handled using parameter maps defined for each grid point, eliminating the need for explicitly stated boundary conditions. The formulation in Cartesian coordinates is expressed as follows:

$$\rho(\mathbf{x})\frac{\partial v_i}{\partial t}(\mathbf{x},t) = \sum_{j=1}^{d}\frac{\partial T_{ij}}{\partial x_j}(\mathbf{x},t) + f_i(\mathbf{x},t) \tag{9}$$

and

$$\frac{\partial T_{ij}}{\partial t}(\mathbf{x},t) = \sum_{j=1}^{d}\sum_{i=1}^{d} C_{ijkl}(\mathbf{x})\frac{\partial v_k}{\partial x_l}(\mathbf{x},t) + \theta_{ij}(\mathbf{x},t), \tag{10}$$

where d is the space dimension. $\mathbf{x}$ and t are the space and time variables. $\rho(\mathbf{x})$ is the mass density and $C_{ijkl}(\mathbf{x})$ is the fourth-order stiffness tensor. The components of the particle velocity field are represented by $v_i(\mathbf{x},t)$, and the components of the stress tensor are $T_{ij}(\mathbf{x},t)$. The force sources are denoted by f_i, while θ_{ij} represents the tensor components of strain rate sources. This formulation based on the stiffness tensor allows equally taking into account solid media and fluid media.

The model must be 3-D since, in porous media, both fluids and solids are interconnected, requiring $d = 3$. To solve for the unknown quantities $v_i(\mathbf{x},t)$ and $T_{ij}(\mathbf{x},t)$, the material properties $\rho(\mathbf{x})$ and $C_{ijkl}(\mathbf{x})$ must be specified. For isotropic materials, $C_{ijkl}(\mathbf{x})$ can be described using two independent parameters, bulk modulus K and shear modulus μ.

For the prismatic cell at the fully discharged state and room temperature, the material properties referenced from the literature are listed in Table 2. The binder/carbon composite is treated as a single material at the micro-scale, referred to as conductive binder, as the carbon exists in the form of nanoparticles. The elastic properties of the conductive binder are estimated based on the measured elastic modulus reported in the literature [67, 68] and an assumed Poisson's ratio of 0.35. This value was selected because typical plastics have a Poisson's ratio of around 0.4, while carbon black exhibits a Poisson's ratio of approximately 0.3.

The model geometry was constructed in an approximate manner due to the limitations of the FDTD method, which operates on a regular spatial grid and offers limited geometric flexibility. Considering the

Table 2: Composition mechanical properties of the prismatic cell

Composition	ρ [kg/m^3]	K [GPa]	μ [GPa]
$LiFePO_4$ [69]	3520	94.3	44.3
Cathode binder [67] (PVDF&Carbon black)	1964	1.78	0.59
Graphite [70]	2260	29.3	12.3
Anode binder [68] (CMC&SBR&Carbon black)	1636	0.56	0.19
PP	900	1.38	0.92
Electrolyte	1270 [71]	2.49^a	

^{a} Derived from measured sound speed of 1400 m/s.

material weight fractions listed in Table 1, the densities provided in Table 2, the cell geometry, and the number of layers revealed by X-ray CT, a spatial step size of 2 μm was chosen to effectively model the microstructures. The active particles ($LiFePO_4$ and graphite) were modeled as cubes with a side length of 16 μm, while the binders were represented as cuboids with dimensions of 8 μm $\times$ 8 μm $\times$ 2 μm, connecting the particles. This approach results in geometric parameters that closely approximate the actual structure, as listed in Table 3.

Table 3: Geometrical parameters in the FDTD model of the prismatic cell

Layer	Thickness [μm]	Number of layers	Material	Volume fraction
Cathode	74	152	$LiFePO_4$	51.9%
			Binder	9.9%
			Electrolyte	38.2%
Anode	56	160	Graphite	52.6%
			Binder	9.7%
			Electrolyte	37.7%
Separator	16	160	PP	50%
			Electrolyte	50%
Al	60	76		
Cu	8	80		

Figure 10 illustrates the geometry of the FDTD model. A representative unit cell was constructed first, which is symmetric with respect to all six surfaces relative to adjacent units. Consequently, the Cu and Al layers within the unit cell are modeled with half of their actual thickness. The solid phase of the separator, made of PP, is modeled as a regular frame structure. Given that the separator is not bonded to the electrodes, additional thin layers with a unit thickness of 2 μm were introduced between the separator and the electrodes to simulate weak interfaces [72, 73, 74, 75]. These thin layers account for the friction forces, ensuring that stresses remain continuous through their thickness. However, due to the potential for sliding, there can be an in-plane displacement discontinuity. To simulate this behavior, the thin layers are assigned the material properties of PP, with the exception of the shear modulus. A very small but non-zero shear modulus, 0.25% of PP's shear modulus, is used in these layers to ensure shear stress continuity while allowing for in-plane displacement discontinuity.

For the simulation of through-thickness transmission, the representative unit and its through-thickness reflection form a repetitive unit, which is then extended in the z-direction. A plane wave source was applied to the top surface of the model in the z-direction, with transmitted waves received on the bottom surface. Due to the symmetry in both geometry and wavefields, symmetric boundary conditions were imposed on the four side surfaces, creating a quasi-1-D model, as illustrated in Figure 10A. Similarly, an in-plane transmission model was constructed, as shown in Figure 10B.

Given the aforementioned material properties, geometries, and boundary conditions, Equations 9 and 10 were solved using the FDTD method, implemented with the freely available third-party software suite SimSonic [66]. This software employs central-difference approximations for the space and time partial derivatives and discretizes spatial and temporal domains over regular grids defined by a temporal step

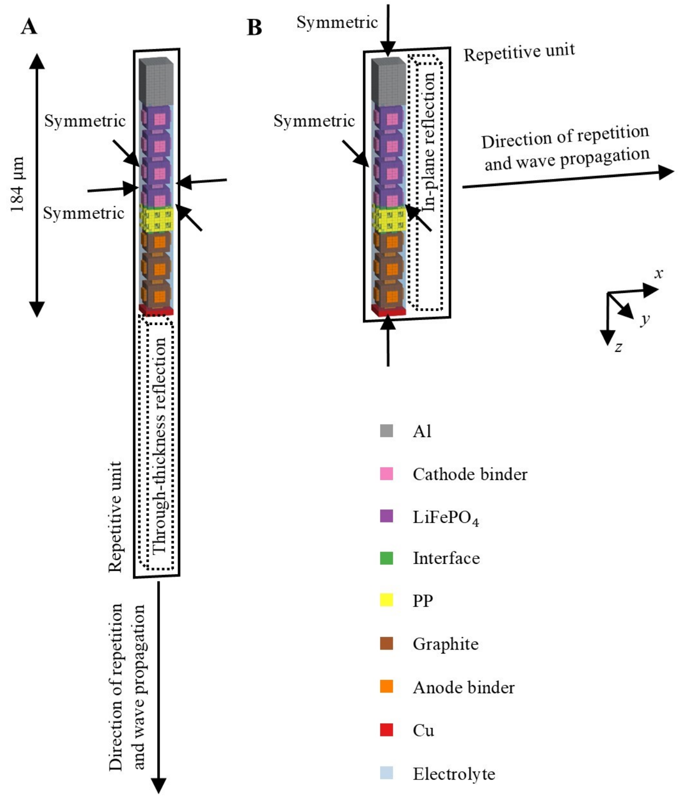

Figure 10: Acoustic simulation models for (A) through-thickness transmission and (B) in-plane transmission.

$\Delta\tau$ and a spatial step Δx. Both the time and spatial steps must be sufficiently small to ensure smooth representations of the computed field. The spatial step was inherently small (2 μm) since the micro-scale structures are being modeled. The time step is determined by the Courant-Friedrichs-Lewy (CFL) condition:

$$\Delta\tau \leq \frac{1}{\sqrt{d}} \frac{\Delta x}{c_{max}}, \tag{11}$$

where c_{max} is the highest sound speed among all sound speeds present in the simulation medium.

Supporting Information

The animated real-time temperature mapping results: Movies S1-S7.

- Movie S1: Video of real-time temperature mapping. This video shows the experimental setup for real-time mapping of internal temperature distribution in a prismatic cell exposed to a 50 ℃ external heat source positioned at the bottom left corner. The temperature evolution is displayed in real-time on the laptop screen, which is the animated version of Figure 4. The video playback is accelerated 64 times for enhanced viewing.
- Movie S2: Temperature evolution during 2 C charge. This GIF displays the temperature evolution within a prismatic cell during a full 2 C charge cycle, followed by a resting stage.
- Movie S3: Temperature evolution during 2 C discharge. This GIF displays the temperature evolution within a prismatic cell during a full 2 C discharge cycle, followed by a resting stage.
- Movie S4: Temperature evolution with poor-contact negative pole. This GIF displays the temperature evolution within a prismatic cell during a full 2 C discharge cycle, followed by a resting stage, under conditions of poor contact at the negative pole.
- Movie S5: Temperature evolution during 3 C charge. This GIF displays the temperature evolution within a prismatic cell during a full 3 C charge cycle, followed by a resting stage.

- Movie S6: Temperature evolution during 3 C discharge. This GIF displays the temperature evolution within a prismatic cell during a full 3 C discharge cycle, followed by a resting stage. It is the animated version of Figure 6.
- Movie S7: Temperature evolution in a larger cell. This GIF displays the temperature evolution within a larger prismatic cell (Model: EVE LF105, rated capacity: 105 Ah) during a full 0.5 C discharge cycle, followed by a resting stage.

Acknowledgements
We gratefully acknowledge support from MOE AcRF Tier 1, RG149/23 and A*STAR (Career Development Fund, project no. C222812020). We also thank Dr. Shuaibin Wan for his valuable feedback on the results.

References

[1] Y. Fu, S. Lu, K. Li, C. Liu, X. Cheng, H. Zhang, *Journal of Power Sources* **2015**, *273* 216.

[2] W. Mei, Z. Liu, C. Wang, C. Wu, Y. Liu, P. Liu, X. Xia, X. Xue, X. Han, J. Sun, et al., *Nature communications* **2023**, *14*, 1 5251.

[3] T. Waldmann, M. Wohlfahrt-Mehrens, *Electrochimica Acta* **2017**, *230* 454.

[4] L. Zhao, M. Zheng, J. Zhang, H. Liu, W. Li, M. Chen, *Journal of Energy Storage* **2023**, *63* 107053.

[5] H. Zhou, C. Fear, R. E. Carter, C. T. Love, P. P. Mukherjee, *Energy Storage Materials* **2024**, *66* 103214.

[6] E. Hosseinzadeh, R. Genieser, D. Worwood, A. Barai, J. Marco, P. Jennings, *Journal of power sources* **2018**, *382* 77.

[7] M. Luo, X. Lin, J. Feng, Z. Ling, Z. Zhang, X. Fang, *Journal of Power Sources* **2023**, *565* 232897.

[8] K. A. Gamra, N. Wassiliadis, C. Allgäuer, M. Lienkamp, *Journal of Energy Storage* **2024**, *84* 110968.

[9] S. Drake, M. Martin, D. Wetz, J. Ostanek, S. Miller, J. Heinzel, A. Jain, *Journal of Power Sources* **2015**, *285* 266.

[10] N. I. Nikolov, A. Chahbaz, F. Hildenbrand, M. Kateri, D. U. Sauer, *Journal of Power Sources* **2024**, 235334.

[11] Z. Guo, Z. Chen, *Journal of Electroanalytical Chemistry* **2015**, *754* 148.

[12] M. Feinauer, M. Wohlfahrt-Mehrens, M. Hölzle, T. Waldmann, *Journal of Power Sources* **2024**, *594* 233948.

[13] H. Maleki, J. N. Howard, *Journal of Power Sources* **2009**, *191*, 2 568.

[14] Y. Ren, H. Zhang, L. Wei, X. Feng, W. Wu, *Journal of Energy Storage* **2024**, *97* 112824.

[15] Y. Jia, P. Zhao, D. P. Finegan, J. Xu, *Advanced Energy Materials* **2024**, 2400621.

[16] X. Feng, M. Ouyang, X. Liu, L. Lu, Y. Xia, X. He, *Energy storage materials* **2018**, *10* 246.

[17] B. Li, M. H. Parekh, R. A. Adams, T. E. Adams, C. T. Love, V. G. Pol, V. Tomar, *Scientific reports* **2019**, *9*, 1 13255.

[18] S. Ma, M. Jiang, P. Tao, C. Song, J. Wu, J. Wang, T. Deng, W. Shang, *Progress in Natural Science: Materials International* **2018**, *28*, 6 653.

[19] M. Steinhardt, J. V. Barreras, H. Ruan, B. Wu, G. J. Offer, A. Jossen, *Journal of Power Sources* **2022**, *522* 230829.

[20] J. Lu, Y. Lyu, B. Chen, C. Wu, *Batteries* **2024**, *10*, 6 184.

[21] Z. Li, J. Zhang, B. Wu, J. Huang, Z. Nie, Y. Sun, F. An, N. Wu, *Journal of Power Sources* **2013**, *241* 536.

[22] B. Wu, Z. Li, J. Zhang, *Journal of The Electrochemical Society* **2014**, *162*, 1 A181.

[23] M. Ghalkhani, F. Bahiraei, G.-A. Nazri, M. Saif, *Electrochimica Acta* **2017**, *247* 569.

[24] M. Mastali, E. Foreman, A. Modjtahedi, E. Samadani, A. Amirfazli, S. Farhad, R. A. Fraser, M. Fowler, *International Journal of Thermal Sciences* **2018**, *129* 218.

[25] Y. Xie, X. He, W. Li, Y. Zhang, D. Dan, K. Lee, J. Liu, *International Journal of Energy Research* **2020**, *44*, 14 11725.

[26] C. He, Q. Yue, M. Wu, Q. Chen, T. Zhao, *International Journal of Heat and Mass Transfer* **2021**, *181* 121855.

[27] X. Gao, Y. Li, H. Wang, X. Liu, Y. Wu, S. Yang, Z. Zhao, M. Ouyang, *Applied Energy* **2023**, *336* 120868.

[28] S. Li, C. Zhang, Y. Zhao, G. J. Offer, M. Marinescu, *Communications Engineering* **2023**, *2*, 1 74.

[29] L. Cloos, T. Wetzel, *Energy Technology* **2025**, 2402409.

[30] A. S. Alujjage, B. S. Vishnugopi, A. Karmakar, D. P. Magee, Y. Barsukov, P. P. Mukherjee, *Advanced Functional Materials* **2025**, 2417273.

[31] T. Heenan, I. Mombrini, A. Llewellyn, S. Checchia, C. Tan, M. Johnson, A. Jnawali, G. Garbarino, R. Jervis, D. Brett, et al., *Nature* **2023**, *617*, 7961 507.

[32] S. Zhu, J. Han, H.-Y. An, T.-S. Pan, Y.-M. Wei, W.-L. Song, H.-S. Chen, D. Fang, *Journal of power sources* **2020**, *456* 227981.

[33] D. Guo, T. Pan, W. Li, R. Zhang, B. Zhao, F. Li, X. Huang, T. Hu, Y. Hu, M. Gao, et al., *Journal of Power Sources* **2025**, *631* 236259.

[34] N. Kisseler, F. Hoheisel, C. Offermanns, M. Frieges, H. Heimes, A. Kampker, *Batteries* **2024**, *10*, 2 41.

[35] Q. Zhang, Y. Wang, Q. Deng, Y. Chu, P. Dong, C. Chen, Z. Wang, Z. Xia, C. Yang, *Angewandte Chemie* **2024**, *136*, 18 e202401716.

[36] W. Jeong, S.-O. Kim, H. Lim, K. Lee, *Journal of Energy Storage* **2024**, *104* 114558.

[37] Y. Zheng, Y. Che, X. Hu, X. Sui, D.-I. Stroe, R. Teodorescu, *Progress in Energy and Combustion Science* **2024**, *100* 101120.

[38] J. Peng, X. Zhao, J. Ma, D. Meng, J. Zhu, J. Zhang, S. Yan, K. Zhang, Z. Han, *eTransportation* **2024**, 100360.

[39] D. Williams, R. Copley, P. Bugryniec, R. Dwyer-Joyce, S. Brown, *Journal of Power Sources* **2024**, *590* 233777.

[40] A. S. Borujerdi, C. Jin, J. Zhu, *Journal of Power Sources* **2024**, *597* 234103.

[41] B. Liu, W. Tong, Y. Cao, J. Li, *Journal of Energy Storage* **2024**, *87* 111434.

[42] T. M. McGee, B. Neath, S. Matthews, O. A. Ezekoye, M. R. Haberman, *Journal of Power Sources* **2024**, *595*, 234035.

[43] N. Duric, P. Littrup, L. Poulo, A. Babkin, R. Pevzner, E. Holsapple, O. Rama, C. Glide, *Medical physics* **2007**, *34*, 2 773.

[44] P. Huthwaite, F. Simonetti, *The Journal of the Acoustical Society of America* **2011**, *130*, 3 1721.

[45] P. Holstein, A. Raabe, R. Müller, M. Barth, D. Mackenzie, E. Starke, *Measurement Science and Technology* **2004**, *15*, 7 1420.

[46] B. Zhu, Q. Zhong, Y. Chen, S. Liao, Z. Li, K. Shi, M. A. Sotelo, *IEEE Transactions on Ultrasonics, Ferroelectrics, and Frequency Control* **2022**, *69*, 7 2352.

[47] Y. Quan, L. Huang, In *Medical Imaging 2007: Ultrasonic Imaging and Signal Processing*, volume 6513. SPIE, **2007** 48–56.

[48] C. Li, N. Duric, P. Littrup, L. Huang, *Ultrasound in medicine & biology* **2009**, *35*, 10 1615.

[49] A. C. Kak, M. Slaney, *Principles of computerized tomographic imaging*, SIAM, **2001**.

[50] S. Ha, K. Lonkar, A. Mittal, F.-K. Chang, *Structural Health Monitoring* **2010**, *9*, 3 247.

[51] F. Polewczyk, J.-M. Leyssale, P. Lafourcade, *Computational Materials Science* **2023**, *220* 112045.

[52] H. Y. Guney, *Journal of Polymer Science Part B: Polymer Physics* **2005**, *43*, 20 2862.

[53] L. Laiarinandrasana, J. Besson, M. Lafarge, G. Hochstetter, *International Journal of Plasticity* **2009**, *25*, 7 1301.

[54] A. A. Wang, D. Persa, S. Helin, K. P. Smith, J. L. Raymond, C. W. Monroe, *Journal of Chemical & Engineering Data* **2023**, *68*, 4 805.

[55] A. Rajwade, A. Rangarajan, A. Banerjee, *IEEE Transactions on Pattern Analysis and Machine Intelligence* **2012**, *35*, 4 849.

[56] Y. Zhang, H.-P. Chan, B. Sahiner, J. Wei, M. M. Goodsitt, L. M. Hadjiiski, J. Ge, C. Zhou, *Medical physics* **2006**, *33*, 10 3781.

[57] W. Van Aarle, W. J. Palenstijn, J. De Beenhouwer, T. Altantzis, S. Bals, K. J. Batenburg, J. Sijbers, *Ultramicroscopy* **2015**, *157* 35.

[58] J. Rao, M. Ratassepp, Z. Fan, *Journal of Applied Physics* **2016**, *120*, 19 194902.

[59] J. Virieux, S. Operto, *Geophysics* **2009**, *74*, 6 WCC1.

[60] J. L. Mueller, S. Siltanen, *Linear and nonlinear inverse problems with practical applications*, SIAM, **2012**.

[61] P. Huthwaite, A. A. Zwiebel, F. Simonetti, *IEEE transactions on ultrasonics, ferroelectrics, and frequency control* **2013**, *60*, 3 603.

[62] E. Y. Sidky, J. H. Jørgensen, X. Pan, *Physics in Medicine & Biology* **2012**, *57*, 10 3065.

[63] G. Jones, P. Huthwaite, *NDT & E International* **2018**, *93* 98.

[64] J. M. J. M. Carcione, *Wave fields in real media: Wave propagation in anisotropic, anelastic, porous and electromagnetic media*, Elsevier, **2007**.

[65] S. Zhang, P. Zuo, X. Yin, Z. Fan, *Journal of Energy Storage* **2024**, *83* 110715.

[66] E. Bossy, Q. Grimal, *Bone quantitative ultrasound* **2011**, 181–228.

[67] A. M. Grillet, T. Humplik, E. K. Stirrup, S. A. Roberts, D. A. Barringer, C. M. Snyder, M. R. Janvrin, C. A. Apblett, *Journal of The Electrochemical Society* **2016**, *163*, 9 A1859.

[68] H. Hu, B. Tao, Y. He, S. Zhou, *Polymers* **2019**, *11*, 9 1500.

[69] T. Maxisch, G. Ceder, *Physical Review B* **2006**, *73*, 17 174112.

[70] Y. Qi, H. Guo, L. G. Hector, A. Timmons, *Journal of The Electrochemical Society* **2010**, *157*, 5 A558.

[71] L. Gold, T. Bach, W. Virsik, A. Schmitt, J. Müller, T. E. M. Staab, G. Sextl, *Journal of Power Sources* **2017**, *343*, 536.

[72] P. B. Nagy, *Journal of Nondestructive evaluation* **1992**, *11* 127.

[73] A. Baltazar, L. Wang, B. Xie, S. Rokhlin, *The Journal of the Acoustical Society of America* **2003**, *114*, 3 1424.

[74] F. Lanza di Scalea, P. Rizzo, A. Marzani, *The Journal of the Acoustical Society of America* **2004**, *115*, 1 146.

[75] B. Hosten, M. Castaings, *The Journal of the Acoustical Society of America* **2005**, *117*, 3 1108.